RESEARCH ARTICLE | OCTOBER 24 2023

Underwater microsecond timescale electrical explosions of aluminum and copper foils

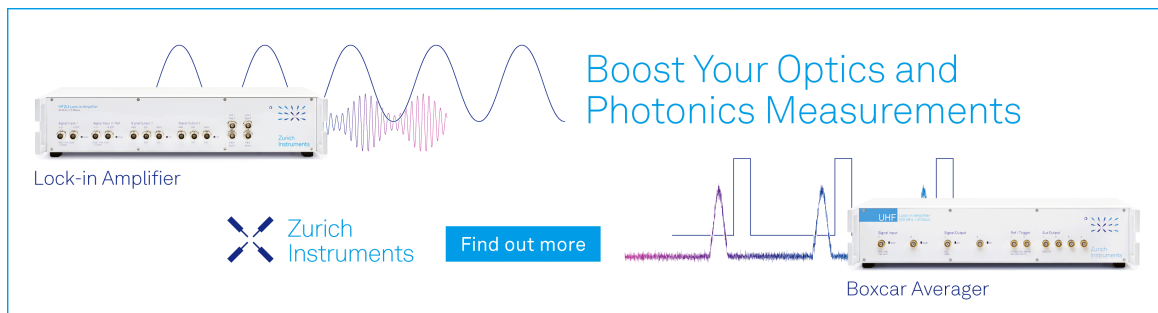N. Asmedianov ✉ (ID) ; R. Grikshtas (ID) ; D. Maler (ID) ; G. Liziakin (ID) ; Ya. E. Krasik (ID)

Check for updates

View Online

Export Citation

17 April 2024 10:59:38

Underwater microsecond timescale electrical explosions of aluminum and copper foils

View Online   Export Citation   CrossMark

N. Asmedianov,[a] R. Grikshtas, D. Maler, G. Liziakin, and Ya. E. Krasik

AFFILIATIONS

Physics Department, Technion—Israeli Institute of Technology, Haifa 3200003, Israel

[a]**Author to whom correspondence should be addressed:** nikitaa@campus.technion.ac.il

ABSTRACT

We present results on underwater electrical explosions of thin aluminum and copper foils using a generator delivering ~200 kA current amplitude, ~0.9 μs rise time pulses. Time-resolved shadow imaging displays the generation of a strong planar shock wave in water in the vicinity of the exploding foil. Using time-resolved spectroscopy, aluminum oxide (AlO) absorption bands were observed in a Planckian-like spectrum, indicating that aluminum combustion starts when aluminum vaporizes. It is also shown that the strongest shock wave is obtained for the largest linear energy deposition rate to the foil.

I. INTRODUCTION

Earlier research showed that underwater electrical wire explosions can be used to study materials at extreme conditions[1–4] and strong shock wave (SSW) generation.[5] For either cylindrical or spherical wire arrays, converging shock waves (shocks) are formed, resulting in the formation of extremely high pressures, temperatures, and densities in the vicinity of shock implosion.[5]

Experiments of underwater electrical explosions of planar wire arrays determined the energy transfer efficiency to the waterflow behind the shock front,[6] the time jitter at the beginning of the wire explosion[7] and aluminum (Al) wire combustion[8,9] which can deliver additional energy to the shock. In experiments with a single Al wire explosion, it was shown that the Planckian self-emission spectrum contains aluminum oxide (AlO) absorption bands typical to aluminum combustion. Decreasing the diameter of an Al wire from 250 to 50 μm decreases the time delay, between the beginning of the discharge and the appearance of the absorption bands, from ~30 to ~1 μs. Additional evidence of Al combustion was obtained in experiments with underwater electrical explosion of a planar Al wire array.[7] Generally, after an array explosion, the shock experiences a rapid decrease in velocity with increasing distance from the array. However, by decreasing the Al wire diameter from 127 μm (array of 40 wires) to 50 μm (array of 50 wires), 6 μs after the initial current discharge, an increase in the shock velocity was

observed.[8] This was explained by the additional energy delivered into the water flow by the combustion of Al.

Early ignition of Al combustion with decreasing wire diameter was explained qualitatively by faster, more efficient mixing and diffusion between the water vapor and the bulk of the exploded aluminum. Thus, it was proposed to study underwater electrical explosion of arrays with smaller diameter aluminum wires. However, decreasing the wire diameter becomes challenging because it is then necessary to significantly increase the number of wires in order to keep the action integral unchanged.[10,11]

Planar strong shocks in water can be used in several studies. For instance, for efficient acceleration of targets[12,13] for studies of hydro-dynamic instabilities;[14] for studies of rarefaction waves and cavitation phenomenon in water.[15] However, in a planar wire array explosion, each individual wire generates a cylindrical shock. These shocks overlap forming a shock which planarity depends on the distance from the array and the initial distance between wires. To obtain a planar shock in the vicinity of the array, where the shock is most intense, one should use a large number of wires of 10–20 μm diameter and sub-mm distance between neighboring wires which becomes technically challenging. In this research, we present results of underwater electrical explosions of aluminum and copper foils aiming for studies of generation of planar shock and the possible combustion of aluminum foils, which can result in additional energy deposition in the generated water flow.

II. EXPERIMENTAL SETUP AND DIAGNOSTICS

The experimental setup is shown in Fig. 1. Experiments were carried out using a μs-timescale high-voltage (HV) generator[12] ($C = 10\,\mu$F, 27 kV charging voltage, stored energy of 3.65 kJ, 250 kA maximal current amplitude with ~1.1 μs rise time on a short-circuit load). The waveforms of the discharge current (I) and voltage (V) were measured using a calibrated self-integrated Rogowski coil (measurement error of ~5%) and a Tektronix P6015A HV divider (measurement error of ~3%), respectively. The inductive voltage $L\frac{dI}{dt}$ was subtracted from the measured value of V to obtain the resistive voltage V_r, where L is the inductance of the foil determined in short circuit shots with non-exploding loads imitating the foil.

In experiments, underwater electrical explosions of Al and Cu foils were studied. The dimensions of the foils (see Table I) were chosen so as to obtain close to critically damped discharge, when most of the energy is deposited into the foil during a time shorter than a quarter period of an underdamped discharge. To achieve this type of discharge, preliminary experiments were carried out where the cross section of Al and Cu foils was estimated using the action current integral[10,11] $S = \left(\frac{1}{h}\int_0^{\tau_{exp}} I^2(t)dt\right)^{0.5}$. For Cu $h \approx 2 \times 10^9 \frac{A^2 s}{cm^4}$ Double and Al $h \approx 0.9 \times 10^9 \frac{A^2 s}{cm^4}$ for a current density below 10^8 A/cm^2. τ_{exp} is the time when the discharge current approaches its maximal amplitude and starts to decrease because of the sharp increase in wire resistivity. The length of the Al and Cu foils was 40 mm which was sufficient to avoid current re-strike accompanied by the formation of a low-resistivity plasma.

Foils were stretched between the grounded (GND) cathode and the high voltage (HV) anode electrodes inside the cylindrical stainless-steel experimental chamber, filled with deionized water [see Fig. 2(a)]. The chamber has two 25-mm-diameter windows located 180° relative to each other and hermetically sealed by 20-mm-thick Perspex plates. A diode pumped continuous wave single-mode laser ($\leq$1.5 W, $\lambda = 532$ nm) was used to backlight the

TABLE I. Parameters of Al and Cu foils.

Foil	Thickness (μm)	Width (mm)	Length (mm)	Mass (g)	No. of atoms
Aluminum	10	50	40	0.054	1.2×10^{21}
	40	10	40	0.043	9.6×10^{20}
Copper	15	28	40	0.15	1.42×10^{21}
	35	8	40	0.1	9.48×10^{20}

exploding foils and the shocks generated in water. The shadow images of the exploding foils and shocks were obtained using two cameras. A streak Optronis Optoscope SC-10 camera (Optronis GmbH), with 100 μm-width entrance slit and a XXRapidFrame (Stanford Computer Optics) camera producing four independent images with a frame duration of 5 ns and with variable time delays between frames. Frame images were obtained along two lines of sight in the parallel and transverse directions relative to the direction of the current flowing through the foil [see Figs. 2(b) and 2(c)]. To suppress self-emission of the exploding foil, two 532-nm interference filters (bandwidth of 1 nm) and a polarizer were used in front of the streak and 4QuikE cameras. The measured shock velocity obtained by the streak image is within an error of ±200 m/s. Self-emission radiation in the visible range of light from the exploded foils was collected by a lens coupled to the optical fiber placed at the top of the experimental chamber at a distance of ~30 cm from the foil [see Fig. 2(a)]. The light transferred by the fiber was focused by lenses to the 100 μm-width slit of the Chromex500si spectrometer coupled at its output to the ICCD 4QuikE (Stanford Computer Optics) camera (see Fig. 1). The spectral resolution of the spectrometer, equipped with grating of
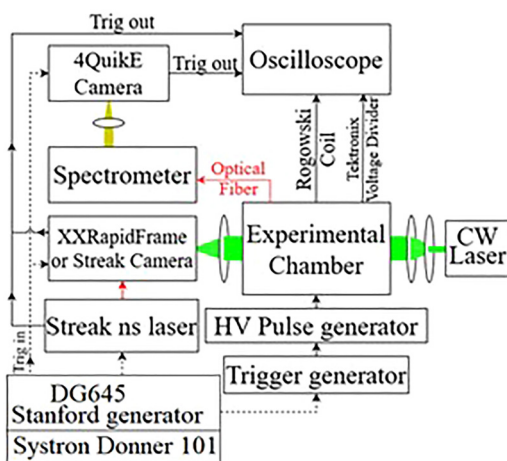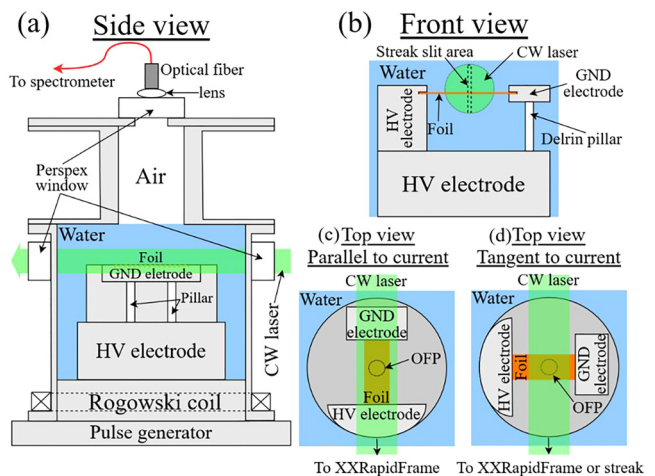
FIG. 1. Experimental setup.

FIG. 2. Sketches of the experimental setup. (a) and (b) side and front, respectively, view when the CW laser is perpendicular to the explosion current. (c) and (d) top view when the CW laser is parallel and perpendicular to the explosion current, respectively.
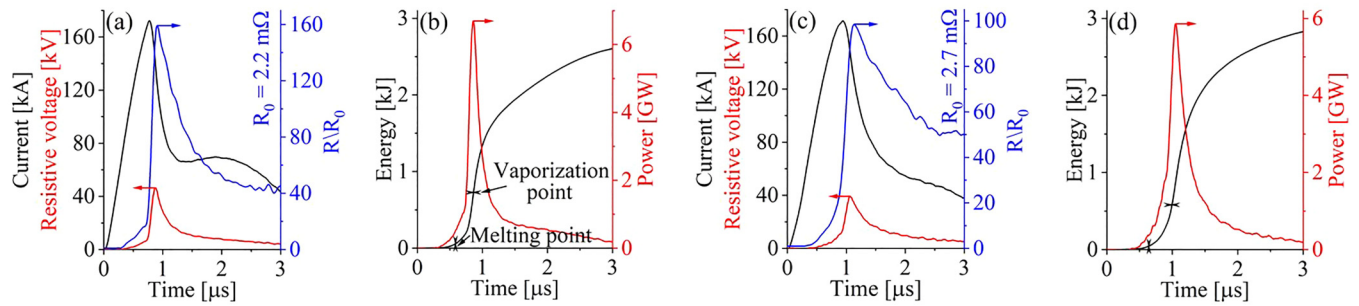
FIG. 3. Waveforms of the current, the resistive voltage and the foil resistance (a, c) together with the deposited power and energy and foil resistance (b, d) obtained in explosions of $10\,\mu$m-thick ×50 mm-width (a, b) and $40\,\mu$m-thick ×10 mm-width (c, d) Al foils. The length of all foils was 40 mm.

300 Gr/mm and calibrated by Oriel spectral lamps, was 1 nm/pixel, with a spectral range of 430–670 nm obtained by the ICCD 4QuikE camera. The frame duration of the camera was of 200 ns in order to obtain reliable spectra.

Waveforms of the current and voltage were acquired by a DPO5104B Tektronix digitizing oscilloscope (bandwidth of 1 GHz, sample rate of 4 GS/s). To synchronize between the pulse power generator and the triggering of the 4QuikE, XXRapid Frame and Optronis streak cameras, a Systron Donner data pulse generator and a DG645 Stanford digital delay generator were used (see Fig. 1). In addition, a pulse NPL52B Thorlabs laser (532 nm, pulse duration of 10 ns), with known time delay relative to the beginning of the discharge current, was used to produce a marker on each streak image. The laser light was transferred by an optical fiber connected at the output of the laser to the input of the streak camera.

III. EXPERIMENTAL RESULTS

A. General parameters of Al and Cu foils explosions

In Figs. 3 and 4, we present waveforms of the current and resistive voltage, obtained in explosions of $10\,\mu$m-thick ×50 mm-width and $50\,\mu$m-thick ×10 mm-width Al foils and $15\,\mu$m-thick ×28 mm-width and $35\,\mu$m-thick ×8 mm-width Cu foils. Additionally, the corresponding deposited power, energy, and foil resistance for each explosion are shown. For the deposited

energy plots, the times corresponding for sufficient energy for melting and vaporization are marked. The latter were calculated using tabulated EOS data for these materials.[16,17] One can see that for $10\,\mu$m-thick ×50 mm-width Al foils, the energy sufficient for vaporization is deposited earlier than all other explosions reported here. Explosions of foils can be characterized as close to critically damped discharges while producing a low-ionized plasma of relatively large resistance of ∼0.3 Ω, similar to the resistance of the Cu wire arrays in earlier research studies.[5,6] Most of the energy, and approximately the same amount, was deposited into Al and Cu foils during ∼700 ns. However, ∼15% larger values of resistive voltage and peak power were obtained for explosions of $10\,\mu$m-thick ×50 mm-width Al and $15\,\mu$m-thick ×28 mm-width Cu foils. It was also observed that the Al foil resistance after peak power decreases, less pronounced for $35\,\mu$m-thick ×8 mm-width Cu foils and not observed at all in explosions of $15\,\mu$m-thick ×28 mm-width Cu foil. The main parameters of these explosions are summarized in Table II. The maximal foil resistance and energy deposition per atom for Al and Cu are very similar. However, the energy density deposition and energy density deposition rate were significantly larger for Al foils and for $35\,\mu$m-thick ×8 mm-width Cu foils. This can lead to faster expansion and higher ionization degree in Al foils and $35\,\mu$m-thick ×8 mm-width Cu foils leading to a decrease in resistance, compared to $15\,\mu$m-thick ×28 mm-width Cu foil explosion. Let us note that the
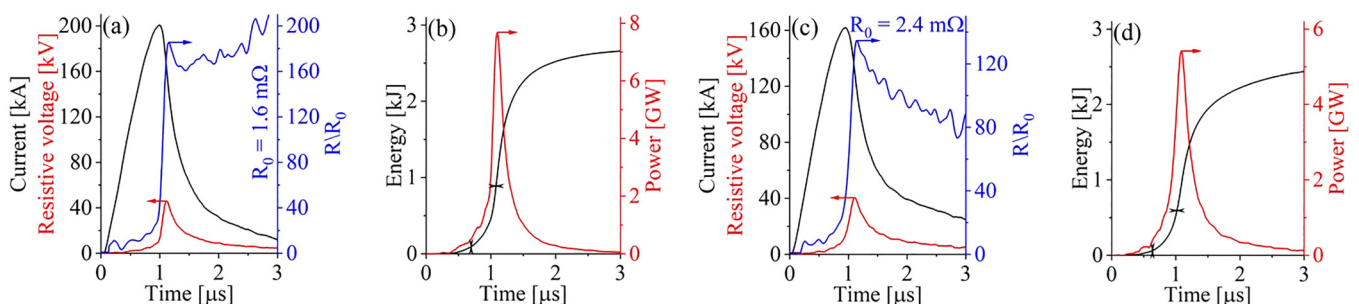
FIG. 4. Waveforms of the current, the resistive voltage and the foil resistance [(a) and (c)] together with the deposited power, energy, and foil resistance [(b) and (d)] obtained in explosions of $15\,\mu$m-thick × 28 mm-width (a) and (b) and $35\,\mu$m-thick × 8 mm-width (c) and (d) Cu foils. The length of foils was 40 mm.

**TABLE II.** Main parameters of Al and Cu foil explosions.

Foil material, thickness/width	Maximal current (kA)	Maximal resistive voltage (kV)	Resistance at maximal voltage (Ω)	Deposited energy (kJ)	Maximal power (GW)	Energy density (kJ/g)/ (eV/atom)	Maximal energy density rate and maximal energy density per unit width $(kJ/(g\,s)) \times 10^7$/ $[kJ/(g\,s\,cm)] \times 10^7$
Al, 10 μm/50 mm	172 ± 9	46.5 ± 1.4	0.33 ± 0.02	2.60 ± 0.16	6.7 ± 0.4	50.2/13.5	9.87/1.94
Al, 40 μm/10 mm	170 ± 9	39.0 ± 1.2	0.26 ± 0.02	2.83 ± 0.17	5.8 ± 0.4	68.5/18.4	10.4/1.04
Cu, 15 μm/28 mm	200 ± 10	46.0 ± 1.4	0.28 ± 0.02	2.66 ± 0.16	7.7 ± 0.4	18.2/11.7	4.06/1.62
Cu, 35 μm/8 mm	162 ± 8	40.5 ± 1.2	0.31 ± 0.02	2.44 ± 0.15	5.4 ± 0.3	25.0/16.1	4.2/5.25

maximal linear energy density deposition rate of the foil was obtained for 35 μm-thick ×8 mm-width Cu foils.

B. Planarity of the shock generated by foil explosions

Shadow frame images of Al and Cu foil explosions and the shocks in water obtained at different times measured from the beginning of the discharge current, for transverse and parallel lines of sight (see Sec. II) are shown in Figs. 5 and 6, respectively. One can see that there is no visible perturbation of the shock front at a distance of ≥1 mm from the foil origin (see Fig. 5). Also, shadow images presented in Fig. 6 show that in spite of the relatively small width (≤10 mm) of the foil, the shock keeps its planarity up to ~2 mm from the origin of the foil. For larger foil widths, the shock planarity is reserved to longer distances, i.e., up

to ~6 mm. These results contradict Comsol frequency domain simulations which show highly non-uniform current density distribution along the foil width with maxima at the edges (see Fig. 7) where the electric field is maximal. This indicates that the explosion should start at the foil edges. However, these simulations do not consider the evolution of the conductivity of the material during the explosion. Indeed, a larger current density at the edges leads to faster heating and consequently to a decrease in the edge conductivity. This leads to the redistribution of the current density resulting in an almost simultaneous explosion of the foil and generation of a uniform shock in water. Let us note here that the intensity of light emission for Al foil explosions was significantly stronger than that obtained for Cu foils the result of intense combustion of Al.
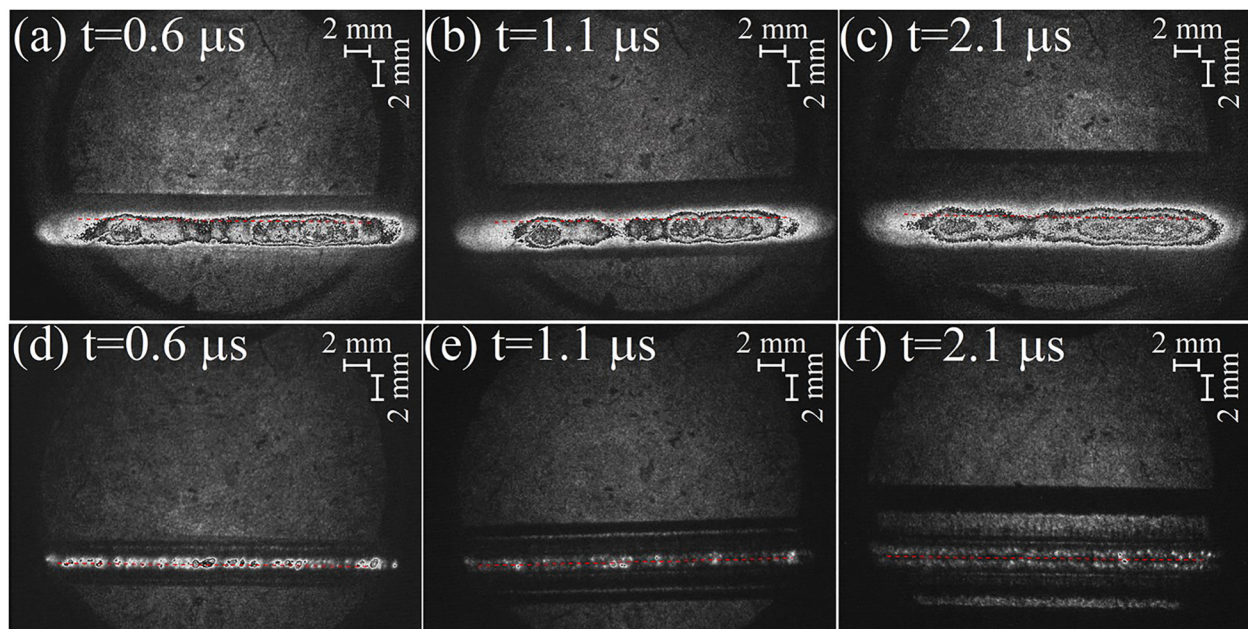
FIG. 5. Shadow images of 40 μm-thick × 10 mm-width Al (a), (b), (c) and 35 μm-thick × 8 mm-width Cu (d), (e), (f) foil explosions. The line of sight is transverse relative to the current direction in the foil. t = 0 at the maximum of the resistive voltage. Each frame is 5 ns long and the magnification of the XXRapidFrame camera was the same for Al and Cu foil explosions.
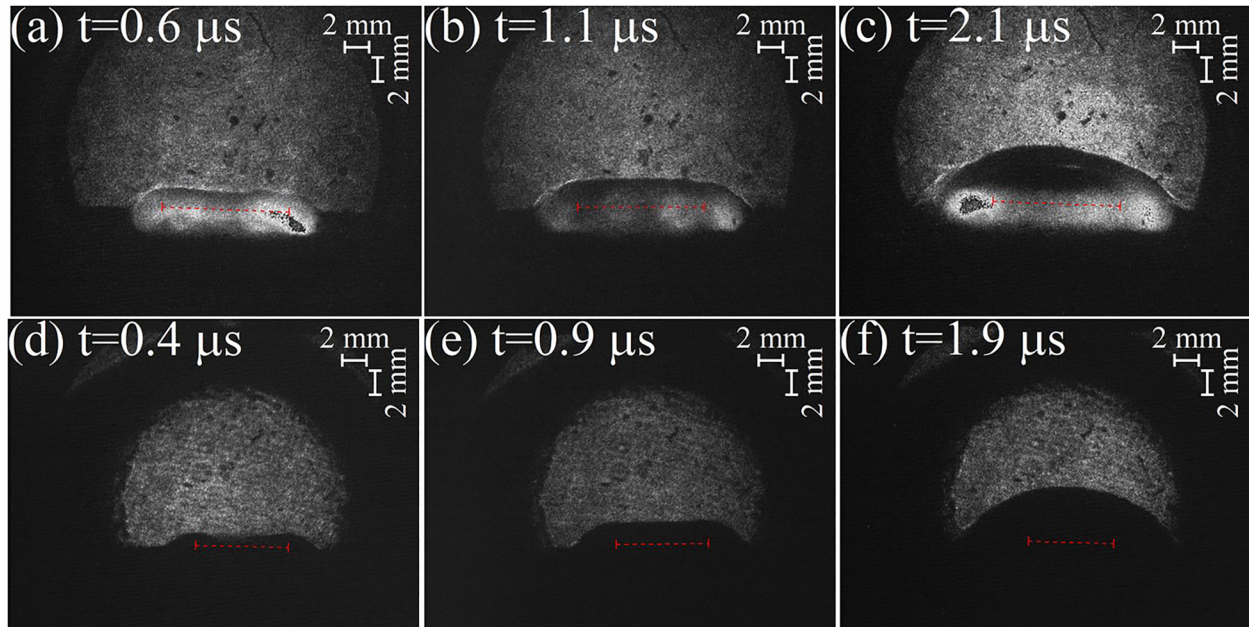
17 April 2024 10:59:38

FIG. 6. Shadow images of 40 μm-thick × 10 mm-width Al (a), (b), (c) and 35 μm-thick × 8 mm-width Cu (d), (e), (f) foil explosions. The line of sight is parallel relative to the current direction in the foil. t = 0 at the maximum of the resistive voltage. Each frame is 5 ns long and the magnification of the XXRapidFrame camera was the same for Al and Cu foil explosions.

C. Velocity of strong shocks generated by Al and Cu wire explosions

Shadow streak images obtained during Al and Cu foil explosions, synchronized with the current and resistive voltage are shown in Fig. 8. The explosion of Al foils is accompanied by several μs long intense radiation compared to ~0.4 μs for Cu. This significant difference is an indirect indication of the combustion of Al. Weak shock generation prior to the maximal amplitude of the discharge current is also observed. These weak shocks, generated due solid–liquid–vapor phase transitions experienced by the foil, were also seen in earlier
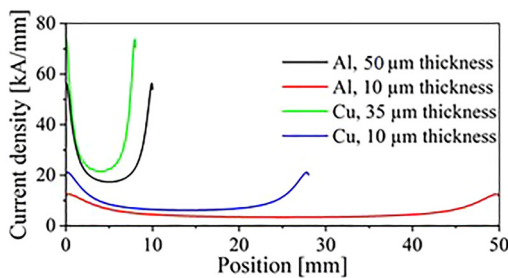

FIG. 7. Results of Comsol frequency domain simulations of the linear current density distribution in Al and Cu foils for a current of 260 kA with a frequency of 380 kHz.
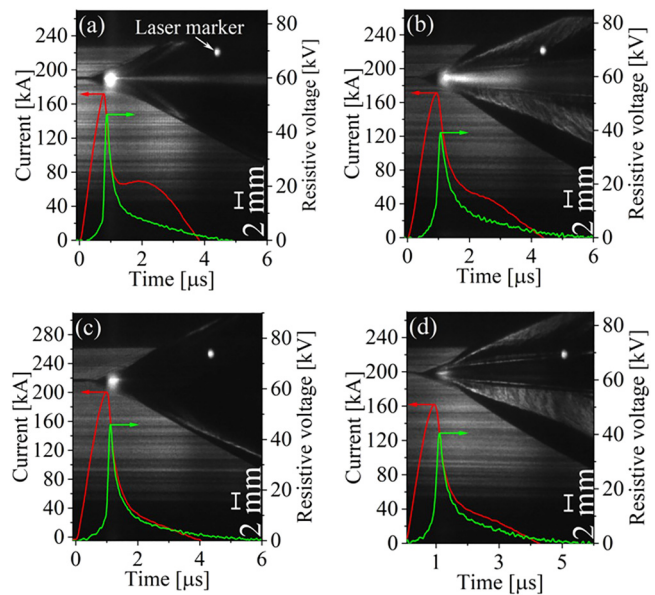

FIG. 8. Shadow streak images obtained for Al and Cu foils explosions and synchronized with current and resistive voltage. 10 μm-thick × 50 mm-width (a) and 40 μm-thick × 10 mm-width (b) Al foils; 15 μm-thick × 28 mm-width (c) and 35 μm-thick × 8 mm-width (d) Cu foils.

17 April 2024 10:59:38

experiments.[8] A strong shock wave (SSW) is generated when the main energy deposition occurs, associated with a fast decrease in the current and increase in the foil resistance. Owing to the weak shock and intense light emission screening at that time, the trajectory of the SSW becomes resolved only after it overtakes the weak shock.

The velocity of the SSW front was calculated using the experimental front trajectories approximated as

$$R(t) = \begin{cases} 0, & \text{if } t < t_0, \\ c_0(t - t_0), & \text{if } t_0 \leq t < t_1, \\ c_0(t_1 - t_0)\left(\dfrac{t + c_1}{t_1 + c_1}\right)^{c_2}, & \text{if } t \geq t_1, \end{cases} \quad (1)$$

where t_0, the weak shock front's beginning, and t_1, the time when the SSW overtakes the weak shock, are determined manually from the streak-image (Fig. 8) and $c_{0,1,2}$ are the constants calculated by the least squares method to fit the SSW shadow image trajectory. In the hydrodynamic simulations, only the SSW was considered

and another function was used to fit the SSW trajectory,

$$R(t) = \begin{cases} 0, & \text{if } t < c_0, \\ c_1(t - c_0)^{c_2}, \end{cases} \quad (2)$$

where c_0, c_1, and c_2 are the constants, determined by the least squares method. The trajectories of SSWs obtained in experiments and by simulations (which are described below) were fitted by functions (1) and (2) with an error of ~5% which results also in a 5% error in the SSW velocity (see Fig. 9).

A two-dimensional (2D) hydro-dynamic (HD) simulation used in earlier research studies[18,19] was applied to study the parameters of the SSW generated by the exploded foil. The experimentally measured energy density deposition rate into the foil is used as an input parameter. This simulation solves at each time step Euler's equation in a Lagrangian form, derived from conservation laws for mass, momentum, and energy,

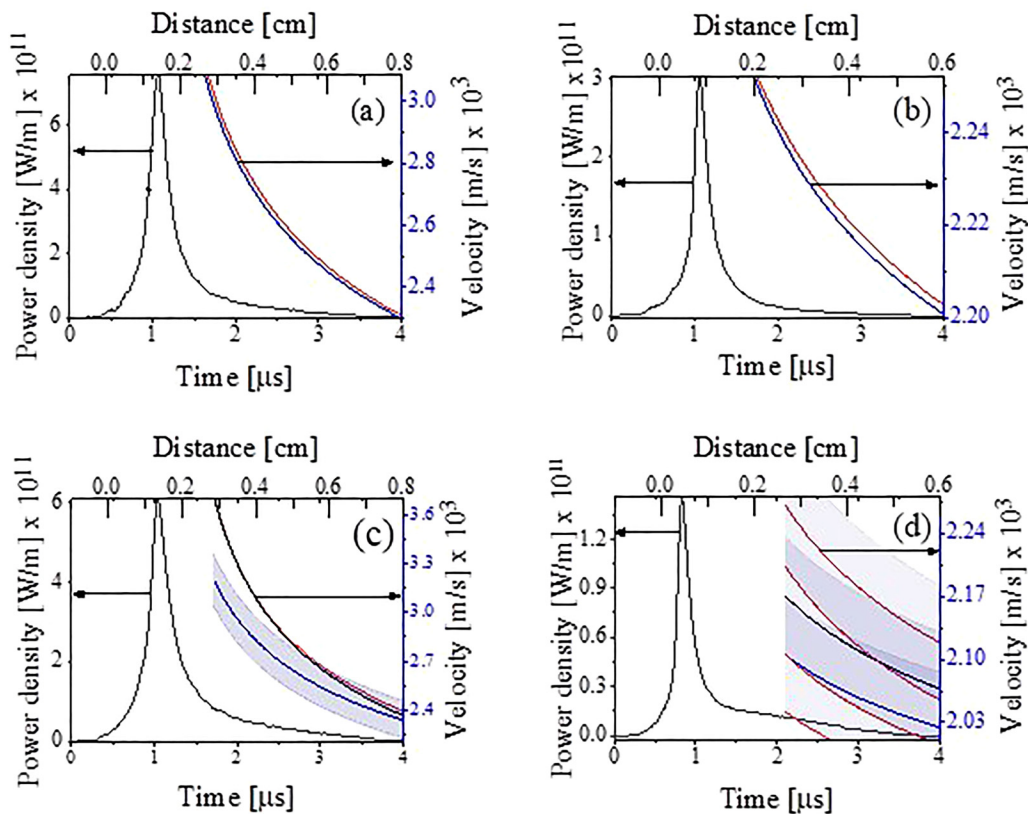$$\frac{\partial \rho}{\partial t} + \vec{\nabla} \cdot (\rho \vec{v}) = 0, \quad (3)$$

FIG. 9. Time dependent SSW velocities in explosions of (a) 35 μm-thick × 8 mm-width and (b) 15 μm-thick × 28 mm-width Cu foils and (c) 50 μm-thick × 10 mm-width and (d) 10 μm-thick × 50 mm-width Al foils. Colors: Red represents the experimental result [Eq. (1)], blue, the result of the simulations without considering Al combustion [Eq. (2)] and black, the result of simulations considering Al combustion during 300 ns [Eq. (2)]. The experimental deposited power per unit foil width is drawn in black.

$$\frac{\partial \rho \vec{v}}{\partial t} + \vec{\nabla}(\rho \vec{v} \cdot \vec{v}) + \vec{\nabla} P = 0, \tag{4}$$

$$\frac{\partial \rho \varepsilon}{\partial t} + \vec{\nabla} \cdot [(\rho \varepsilon + P)\vec{v}] = 0. \tag{5}$$

Here, ρ, ε, $\vec{v}$, and P are the density, internal energy, velocity, and pressure, respectively. Equations (3)–(5) are coupled to the SESAME equation of state (EOS) tables[20] for water, air, copper, and aluminum, such that $P = P(\rho, \varepsilon)$ and $T = T(\rho, \varepsilon)$. In the simulation, space is divided into a triangular mesh, assigning each triangle the corresponding material property. The vertices of each triangle are dislocated according to the sum of forces acting on its edge, changing its area. The density and internal energy are then calculated, enabling the estimation of pressure and temperature in water and foil according to the EOS tables.

In Fig. 9, we show experimental and 2D HD numerically simulated velocities of SSWs generated by explosions of Cu and Al foils together with the experimentally deposited power per unit width of the foils. One can see that the experimental and simulated shock velocities agree for Cu foil explosions [see Figs. 9(a) and 9(b)] which indicates that the EOS and the experimentally measured energy density deposition rate into the foils are correct. In Figs. 9(c) and 9(d), the SSW velocities for Al foil explosion are presented, and one can see also simulated SSW velocities when Al combustion is considered. At present, we do not know the temporal evolution of Al combustion for the conditions realized during foil explosion. Therefore, following qualitative images of the light emission [see Figs. 8(a) and 8(b)], it was assumed that the main part of the combustion energy can probably be deposited into the foil during $\leq 1\,\mu s$ starting at the maximum of the discharge current. A combustion energy of $\sim 700\,J$, for complete Al combustion is $\sim 16\,kJ/g$, which was added artificially in the simulations, to the electrical energy deposited into the Al foil[17] and distributed uniformly in time during 1, 0.6, 0.3, and $0.1\,\mu s$. This inclusion resulted in satisfactory agreement between the experimental and simulated SSW velocities only when this
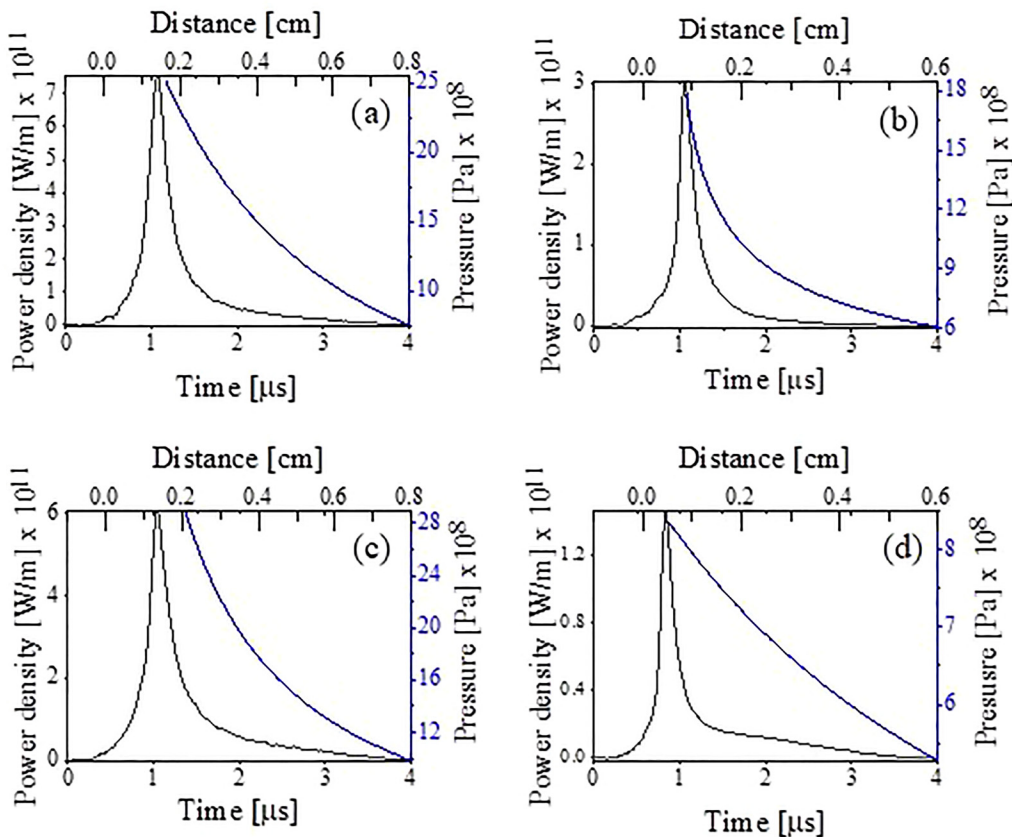
FIG. 10. Simulated temporal and spatial dependence of the pressure behind the shock front for (a) $35\,\mu m$-thick $\times$ 8 mm-width and (b) $15\,\mu m$-thick $\times$ 28 mm-width Cu foils; (c) $50\,\mu m$-thick $\times$ 10 mm-width (d) $10\,\mu m$-thick $\times$ 50 mm-width Al foils. For Al foils, the 700 J energy deposition into the foil during 300 ns after the maximum of the discharge current is added in the simulation as explained.
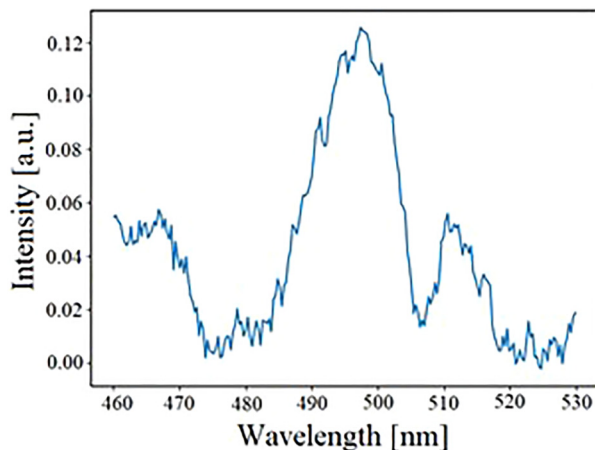
FIG. 11. Absorption spectrum obtained during $10\,\mu$m-thick $\times 50$ mm-width Al foil explosion. The frame duration is 200 ns and the time delay relative to the discharge current's beginning is $1.2\,\mu$s.

additional energy is deposited into the foil during 300 ns [see Figs. 9(c) and 9(d)]. The highest SSW velocity is obtained for $40\,\mu$m-thick $\times 10$ mm-width Al foil explosion in spite that the power density deposition per unit length is smaller than that for $35\,\mu$m-thick $\times 8$ mm-width Cu foil explosion. This indicates that the Al foil combustion which leads to additional energy input into the water flow, is very fast (hundreds of ns). In Fig. 9(c) we draw the SSW velocities obtained in experiment (red curve) and the simulated values without (blue curve with 5% error shaded) and with Al combustion (black curve) included shaded 5% error. One can see that only for 300-ns-duration Al combustion experimental and simulated SSW velocities overlap.

In Fig. 10, simulated temporal and spatial distribution of the pressure behind the SSW front for Cu and Al foil explosions are presented. The highest pressure was obtained for $40\,\mu$m-thick $\times 10$ mm-width Al foil explosions reaching 2.8×10^9 Pa at the distance of 0.2 cm from the foil origin. For a $35\,\mu$m-thick $\times 8$ mm-width Cu foil explosion, in spite of larger linear energy density rate deposition, the pressure at that distance was 2.5×10^9 Pa. Additionally, the results of simulations showed that the maximal temperature in foils is realized for explosions of $15\,\mu$m-thick $\times 28$ mm-width for Cu and $10\,\mu$m $\times 50$ mm Al foils reaching 20 kK and 30 kK, respectively.

Using the spectroscopic setup described in Sec. II, Planck-like radiation with AlO absorption band spectra were obtained at different time delays τ_d relative to the beginning of the discharge current. In Fig. 11, one can see an example of absorption spectral bands of the AlO obtained during a $10\,\mu$m-thick $\times 50$ mm-width Al foil explosion. This spectrum is similar to that obtained in earlier research studies[8] where explosions of single Al wires were studied and the absorption bands are related to aluminum combustion accompanied by AlO formation. Similar spectra but less intense were obtained for a $40\,\mu$m-thick $\times 8$ mm-width Al foil explosion. This spectrum

becomes resolvable at $\tau_d \geq 0.9\,\mu$s when the discharge current reaches its maximal amplitude and starts to decrease due to the formation of a low-conductivity plasma. At $\tau_d \geq 2.5\,\mu$s, the absorption spectrum becomes unresolvable. Thus, one can consider that the most intense combustion occurs during $2.5\,\mu s \geq \tau_d \geq 0.9\,\mu$s. The best fit for Planck-like radiation obtained at $\tau_d = 1.3 \pm 0.1\,\mu$s for $10\,\mu$m-thick $\times 50$ mm-width and $40\,\mu$m-thick $\times 10$ mm-width Al foils explosions result in $\sim 5500 \pm 300$ K and $\sim 4200 \pm 200$ K, respectively. Results of 2D HD simulations without and with inclusion of the combustion energy showed that at this time the temperatures of a $10\,\mu$m-thick $\times 50$ mm-width Al foil is 23 kK and 30 kK and for a $40\,\mu$m-thick $\times 10$ mm-width Al foil are 30 kK and 34 kK, respectively. This contradiction can be related to the formation of a few μm thick dense plasma layer in the vicinity of the exploding foil the result of the absorption of intense radiated UV from the foil.[17]

IV. SUMMARY

Experiments of underwater electrical explosions of Al and Cu foils show that this approach can be successfully used to generate planar strong shocks. The higher current density at the side edges of the foil typical for this geometry is less pronounced due to faster increase in the resistance at those locations leading to current re-distribution. It was shown that the strongest shock is generated for $40\,\mu$m-thick Al foil explosions characterized by the largest linear power density deposition and the largest energy density deposited per atom. The results of 2D HD simulations and estimates using polytropic EOS for water[21] show that the pressure and water density behind the shock front reaches $\sim 2\times 10^9$ Pa and $\sim 1.34\times 10^3$ kg/m^3, respectively. Significantly stronger and longer light emission is obtained for Al foil explosion compared to Cu foil explosions. This observation together with the measured AlO spectral absorption bands indicate that intense Al combustion starts when the wire experiences vapor – high-resistivity plasma transition and fast expansion accompanied by its mixture with water. In earlier studies,[22,23] it was found that ~ 10 kJ/g is necessary for initiating Al material combustion which results in ~ 15 kJ/g energy due to the exothermic reaction $2Al + 3H_2O \rightarrow Al_2O_3 + 3H_2$. In our experiments with Al foil explosion, deposited energy of ~ 10 kJ/g was realized when the vaporization started, coinciding with the maximum of the discharge current and appearance of intense light emission.

AUTHOR DECLARATIONS
Conflict of Interest

The authors have no conflicts to disclose.

Author Contributions

N. Asmedianov: Data curation (equal); Formal analysis (equal); Funding acquisition (equal); Investigation (equal); Methodology

(equal); Project administration (equal); Software (equal); Visualization (equal); Writing – original draft (equal); Writing – review & editing (equal). **R. Grikshtas:** Data curation (equal); Formal analysis (equal); Funding acquisition (equal); Investigation (equal); Resources (equal); Validation (equal); Visualization (equal); Writing – original draft (equal); Writing – review & editing (equal). **D. Maler:** Resources (equal); Validation (equal); Writing – review & editing (equal). **G. Liziakin:** Data curation (equal); Software (equal); Validation (equal); Writing – review & editing (equal). **Ya. E. Krasik:** Conceptualization (equal); Investigation (equal); Methodology (equal); Project administration (equal); Resources (equal); Supervision (equal); Validation (equal); Writing – original draft (equal); Writing – review & editing (equal).

DATA AVAILABILITY

The data that support the findings of this study are available from the corresponding author upon reasonable request.

REFERENCES

[1] V. E. Fortov and I. T. Iakubov, *The Physics of Non-Ideal Plasma* (World Scientific, Singapore, 2000).

[2] A. W. DeSilva and J. D. Katsouros, Phys. Rev. E **59**, 3774 (1999).

[3] A. W. DeSilva and H.-J. Kunz, Phys. Rev. E **49**, 4448 (1994).

[4] J. Stephens, J. Dickens, and A. Neuber, Phys. Rev. E **89**, 053102 (2014).

[5] Y. E. Krasik, S. Efimov, D. Sheftman, A. Fedotov-Gefen, O. Antonov, D. Shafer, D. Yanuka, M. Nitishinskiy, M. Kozlov, L. Gilburd, G. Toker, S. Gleizer, E. Zvulun, V. T. Gurovich, D. Varentsov, and M. Rodionova, IEEE Trans. Plasma Sci. **44**, 412 (2016) and references therein.

[6] S. Efimov, V. T. Gurovich, G. Bazalitski, A. Fedotov, and Y. E. Krasik, J. Appl. Phys. **106**, 073308 (2009).

[7] A. Rososhek, S. Efimov, A. Virozub, D. Maler, and Y. E. Krasik, Appl. Phys. Lett. **115**, 074101 (2019).

[8] A. Rososhek, S. Efimov, A. Goldman, S. V. Tewari, and Y. E. Krasik, Phys. Plasmas **26**, 053510 (2019).

[9] T. Frost, B. M. Novac, D. Danilov, and P. Senior, Propellants, Explos., Pyrotech. **48**, e202300001 (2023).

[10] V. S. Sedoi, G. A. Mesyats, V. I. Oreshkin, V. V. Valevich, and L. I. Chemezova, IEEE Trans. Plasma Sci. **27**, 845 (1999).

[11] V. I. Oreshkin, S. A. Barengol'ts, and S. A. Chaikovsky, Tech. Phys. **52**, 642 (2007).

[12] D. Maler, S. Efimov, and Y. E. Krasik, J. Appl. Phys. **131**, 074902 (2022).

[13] S. Efimov, A. Fedotov, S. Gleizer, V. T. Gurovich, G. Bazalitski, and Y. E. Krasik, Phys. Plasmas **15**, 112703 (2008).

[14] J. Strucka, B. Lukic, M. Koerner, J. W. D. Halliday, Y. Yao, K. Mughal, D. Maler, S. Efimov, J. Skidmore, A. Rack, Y. Krasik, J. Chittenden, and S. N. Bland, Phys. Fluids **35**, 044108 (2023).

[15] D. Maler, S. Efimov, M. Liverts, S. Theocharous, J. Strucka, Y. Yao, W. Proud, A. Rack, B. Lukic, S. N. Bland, and Y. E. Krasik, Phys. Plasmas **29**, 063502 (2022).

[16] See https://www.nist.gov/mml/acmd/trc/web-thermo-tables-wtt/nist-srd-wtt-202-lite for "NIST database."

[17] A. Rososhek, S. Efimov, S. V. Tewari, D. Yanuka, and Y. E. Krasik, Phys. Plasmas **25**, 102709 (2018).

[18] M. Kozlov, V. T. Gurovich, and Y. E. Krasik, Phys. Plasmas **20**(11), 112701 (2013).

[19] D. Maler, R. Grikshtas, S. Efimov, L. Merzlikin, M. Liverts, M. Kozlov, and Y. E. Krasik, Phys. Plasmas **30**, 022710 (2023).

[20] S. Lyon and J. Johnson, Sesame: The Los Alamos National Laboratory Equation of State Database (1992).

[21] A. Fedotov, D. Sheftman, V. T. Gurovich, S. Efimov, G. Bazilitski, Y. E. Krasik, and V. I. Oreshkin, Phys. Plasmas **15**, 082704 (2008).

[22] W. M. Lee, J. Appl. Phys. **69**, 6945 (1991).

[23] A. K. M. Swamy and E. Shafirovich, in *Proceeding of the 8th U.S. National Combustion Meeting* (Curran Associates, Inc., 2013), p. 0124.

17 April 2024 10:59:38